Effect of processing parameters on the microstructure and density of LPBF processed CoCrMo

Marné van Niekerk[1,2*] and *Thorsten H.* Becker[2,3,4]

[1]Department of Mechanical Engineering, North West University, South Africa.
[2]Centre for Materials Engineering, University of Cape Town, South Africa.
[3]Department of Mechanical and Mechatronic Engineering, Stellenbosch University, South Africa
[4]eNtsa, Nelson Mandela University, South Africa

Abstract. Laser Powder Bed Fusion (LPBF) is an additive manufacturing technique highly sensitive to processing parameters, significantly influencing the resulting porosity, microstructure and mechanical properties of components. This study examines the relationship between Volumetric Energy Density (VED), defect formation, and microstructural characteristics in LPBF-manufactured Co-28Cr-6Mo alloy. Twenty-four specimens produced via LPBF were evaluated utilising Archimedes' principle for density measurements, complemented by Optical Microscopy (OM), Scanning Electron Microscopy (SEM), and X-ray Diffraction (XRD). The results provide insights into how variations in LPBF parameters affect porosity levels and microstructural evolution, contributing toward optimising processing conditions for enhanced material performance.

1 Introduction

The benefits of Additive manufacturing (AM) are especially applicable to low-volume manufacturing industries, such as those that produce custom-manufactured parts [1]. Laser Powder Bed Fusion (LPBF), a metal AM process, has gained greater attention in the biomedical and aerospace industries as a result of its higher dimensional accuracy and compatibility with a wide variety of alloys [2-4].

One alloy processed using LPBF, commonly used in the biomedical industry, is Cobalt Chrome Molybdenum (CoCrMo). The application of CoCrMo in the biomedical field varies from dental applications to orthopaedic implants due to its high corrosion and fatigue resistance, good wear properties, and good biocompatibility [5]. Utilising LPBF to process CoCrMo for dental and orthopaedic implants enables the production of complex structures, porous structures, and patient-specific implant designs that enhance osseointegration and vascularisation, as well as reduce manufacturing time[6-16].

Despite the potential offered by CoCrMo alloys processed via LPBF, the influence of process parameters on the microstructure remains inadequately understood. LPBF involves melting metal powder using a high-speed laser beam, inducing rapid solidification through a

* Corresponding author: marne.vanniekerk@nwu.ac.za

non-equilibrium metallurgical process governed by complex heat, mass, and momentum transfer phenomena [17]. These unique thermal conditions drive localised grain growth and contribute to the formation of intricate microstructures, exhibiting a fine dendritic microstructure with columnar grains aligned in the direction of the building direction [18]. In addition to microstructural evolution, LPBF is prone to defects such as lack of fusion (LOF) caused by insufficient energy input, keyholing pores formed due to instability during solidification, microcracks resulting from high thermal gradients, and balling, which occurs when low scan speeds cause the molten material to contract into isolated droplets. These defects can significantly impact the mechanical performance [19]. Given that over 130 processing parameters influence the final part quality, research typically focuses on four key variables: laser power (P), scan speed (v), layer thickness (t), and hatch distance (h) [20]. These parameters collectively define the Volumetric Energy Density (VED), a key metric characterising energy input during LPBF fabrication, determined through Equation 1 [21].

$$\text{VED} = \frac{P}{v\,t\,h}$$

The VED is typically used to broadly determine the operating window where certain types of porosities occur; too low a VED will produce a LOF pores comprising unmelted powder, while too high a VED will result in keyholing [22]. Open literature indicates that a typical VED range of between 85 – 150 J/mm^3 should provide a relative density (RD) of >99 % for CoCrMo [22, 23].

CoCrMo undergoes allotropic transformation when heated, shifting from hexagonal close-packed HCP (ε) to face-centred cubic FCC (γ) [24]. Due to the complexity of CoCrMo alloying system, results reported in literature regarding the as-built microstructure have been inconsistent. Various phases have been reported to exist in the as-built state; however, the majority indicate that, owing to the rapid solidification associated with LPBF, only the γ phase is present [25-27]. Additional research suggests that while the γ phase is dominant, a non-negligible fraction of the ε phase may also present in the matrix [22, 28]. Conversely, some studies contend that the ε phase is the predominant phase in the as-built condition [29]. Liu *et al.* [30] investigated the effect of processing parameters on the phase composition of a CoCr alloy and found that parameters having slower scan speeds and lower laser powers resulted in a slight increase in the ε phase. Conversely, Liu *et al.* found that parameters having higher scan speeds and laser powers promoted retention of the γ phase due to the suppression of phase transformation at high cooling rates. Tonelli *et al*. [22] examined the relationship between the variance in VED and the density, microstructural features, and hardness of CoCrMo, which revealed that the grain growth does not align with the heat flux direction; instead, it follows a preferential crystallographic orientation, typically in the <100> family, which is aligned closely with the thermal gradient direction. However, it is possible to achieve a preferential <111> orientation for increased ductility by modifying the laser scanning direction and adjusting the scanning pattern across layers. The study also indicated that the amount of ε-phase decreases at higher VED, suggesting that varying thermal gradients associated with different VED levels may either facilitate or hinder the transformation from γ to ε. In addition to influencing microstructure and phase formation, LPBF process parameters play a critical role in the development of residual stresses. These stresses originate from the steep thermal gradients and rapid solidification inherent to the LPBF process, leading to non-uniform thermal contraction and constrained shrinkage across layers [31].

Understanding how VED affects the microstructural features of LPBF CoCrMo will provide a better insight into parameter optimisation that not only focuses on porosity content, but also on the microstructure of the as-built alloy. By clarifying these parameters, defect and microstructure links, the study aims to provide a broader understanding beyond empirical

"print-and-test" routines and toward rational, model-driven optimisation of biomedical Co-Cr-Mo components.

2 Material and methods

2.1 Material and equipment

All samples were manufactured using commercially available gas-atomised ASTM75 standard CoCrMo alloy, produced by Praxair (Connecticut, United States), in a nitrogen gas environment, utilising an ORLAS Creator (2Build, Germany) unit equipped with a 250 W Yb: Fibre laser. The chemical composition of the material is illustrated in Table 1, and was compiled using ICP-OES. The particle size distribution of the sample was determined to be D_{10} = 23.15 µm, D_{50} = 35.84 µm and D_{90} = 50.16 µm. A scanning electron microscopy (SEM) image was taken to corroborate the findings, as illustrated in Figure 1 below.

Table 1. Chemical analysis of CoCrMo Praxair powder

Element	Co	Cr	Mo	Fe	Mn	Si	Ni	Al
% Value	Balance	28.7	6.25	0.47	0.15	0.5	0.25	0.12
ASTM75 % (min – max)		27 - 30	5-7	0-0.75	0.5-1	0.5-1	0-0.5	0-0.1

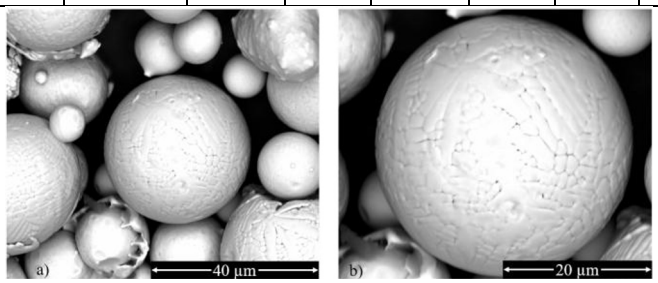

Fig. 1. SEM image of CoCrMo powder a) 4000 x magnification b) 7000 x magnification.

The laser beam spot size, layer thickness, and rotation between successive layers were maintained at 120 µm, 25 µm, and 67 degrees, respectively. The design space was constructed with statistical software StatEase's D-Optimal design (version 23.1.4, Minnesota, USA) of experiment and comprised of the power ranging from 95 to 200 W, a scan speed between 400 to 900 mm/s and a hatch spacing values of 0.04, 0.05 and 0.06 mm, with the VED constrained between 80 and 250 J/mm^3. The specific combinations of P in W, v in mm/s, and h in mm are detailed in the Table 3 listed under Annexures. Figure 2 illustrates the design space.

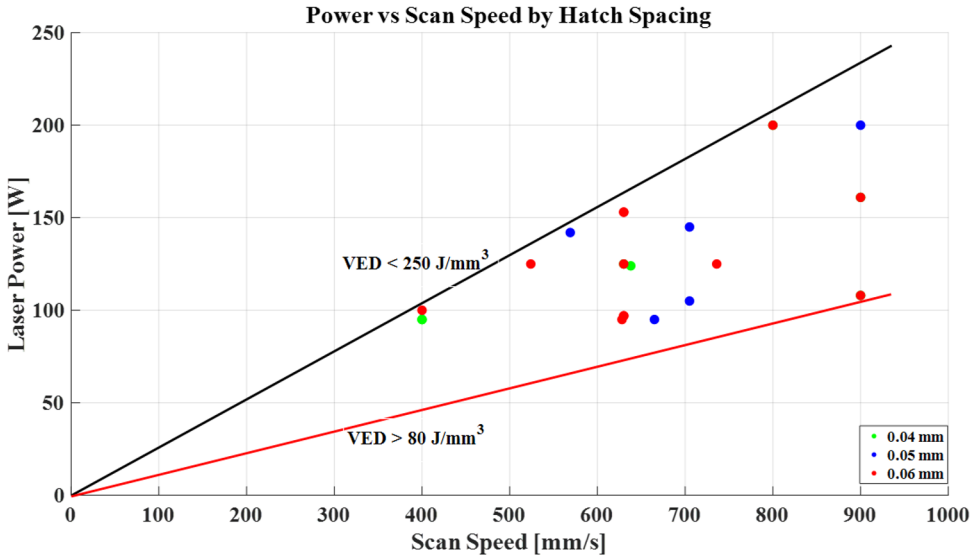

Fig. 2. Design space with green dots = 0.040 m hatch distance, blue dots = 0.050 mm hatch distance and red dots = 0.060 mm hatch distance.

A total of 24 cylindrical samples, each measuring 10 mm in diameter and 15 mm in height, were produced in the building direction (BD) as illustrated in Figure 3 below. The post-manufacturing of the samples consisted of removing the samples from the build plate with an EDM wire cutter (Suzhou Sanguang Science & Technology Co., LTD, China). No heat-treatments were applied after fabrication.

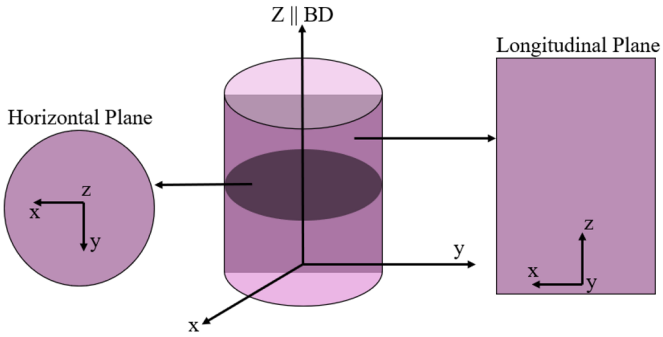

Fig. 3: Schematic illustration of sample building orientation and sectional planes.

2.2 Density measurement

Following fabrication, the densities of the samples are determined using Archimedes' principle, as specified in ASTM B311. For each sample, the median, first quartile, and third quartile of five measurements were calculated. The median value was then used in the results and discussion sections. These measurements were taken using an Adam Luna analytical balance scale from Johannesburg, South Africa, with a sensitivity of 0.0001 g. The samples were polished to reduce any surface tension that might affect the reading. Furthermore, the liquid used was pure acetone to reduce surface tension, as indicated in the literature [32].

The RD in % of the samples was calculated by Equation 2 with the baseline density of 8.4 g/cc. The RD values for each sample were inserted into statistical software StatEase, with which the design space was also constructed through D-Optimal design. An ANOVA analysis is then applied to the results to determine which parameter (P, v, h) has a significant influence on the result.

$$\mathrm{RD} = \frac{\rho_{measured}}{\rho_{baseline}}$$

2.3 Microstructural analysis

After the RD's of all the samples were determined, a subset of six samples was selected that produce a high RD, above 99.6 %, with varying VED, to investigate what effect each parameter set had on the microstructure. Specifically, there were two samples with a low VED (80 - 120 J/mm³), two at medium VED (121 - 199 J/mm³), and two at high VED (200 - 250 J/mm³). These samples labelled according to the respective parameter set, P100S200H40, which indicates a P of 100 W, a v of 200 mm/s, and a h of 0.040 mm.

For all microstructural analysis, the sample's horizontal plane, as illustrated by Figure 3 above, was polished with Struers' (Copenhagen, Denmark) water-based diamond suspension with a grit size of 9 and 3 µm. The samples were finalised to a mirror finish using Struers' MD-Chem polishing cloth along with an oxide lubricant, Struers' OP-U with a grit size of 0.04 µm, in accordance with Struers' guidelines for cobalt alloys [33]. Optical microscopy (OM) and SEM micrographs were taken using an Olympus BX43 (Tokyo, Japan) and FEI Quanta FEG 250 (Oregon, USA), respectively. X-ray diffraction (XRD) was conducted on selected data points to determine if there is any change in the microstructure of the samples using a PANalytical X'Pert Pro system (Worcestershire, UK) employing Co-Kα radiation (λ = 0.178901 nm).

3 Results

3.1 Density

The RD for all samples is presented in Table 4 in the annexures, with the relationships between RD, P, v, and h depicted in Figure 4 below. ANOVA results indicate that P has the most significant influence on RD, with an F-value of 4.77 and p = 0.0465, while v and h show lower significance (F = 1.38 and 2.53; p = 0.05 and 0.13, respectively). When comparing the processing parameters of two samples that have the same v (900 mm/s) and h (0.06mm) but differ in P (161 W and 108 W), the impact of P on RD is evident. Sample P161S900H60 has a VED of 119 J/mm³, while sample P108S900H60 has a VED of 80 J/mm³. The lower P (108 W) contributes to an RD of 98.11 %, whereas the increase in P (161 W) resulted in an RD of 99.79%, thus supporting the ANOVA analysis.

Figure 4 a) shows a clear threshold in P; below 110 W, RD remains low (98–98.40%), whereas above this value, densification improves markedly (>99.60%) and stabilises. This is attributed to insufficient melting at low power, leading to LOF, which is mitigated as energy input increases. Figure 4 b) reveals a reverse threshold for v; RD is high up to 600 mm/s but is highly scattered at 700–900 mm/s. High v reduce laser–powder interaction time, limiting melting and increasing LOF. In Figure 4 c), there is no discernible trend in the data, as all values contribute to both low and high RD, suggesting that the variable h alone does not significantly influence RD. Nevertheless, it would be anticipated that lower values would correspond to a higher RD. Collectively, low RD clusters (98–98.4%) are consistently

observed for low P (<110 W), high v (>700 mm/s), and wide h (>0.05 mm), indicating under-melting and poor fusion. In contrast, combinations such as P > 110 W, $v \leq 600$ mm/s, and $h \leq 0.045$ mm result in improved RD due to sufficient energy input.

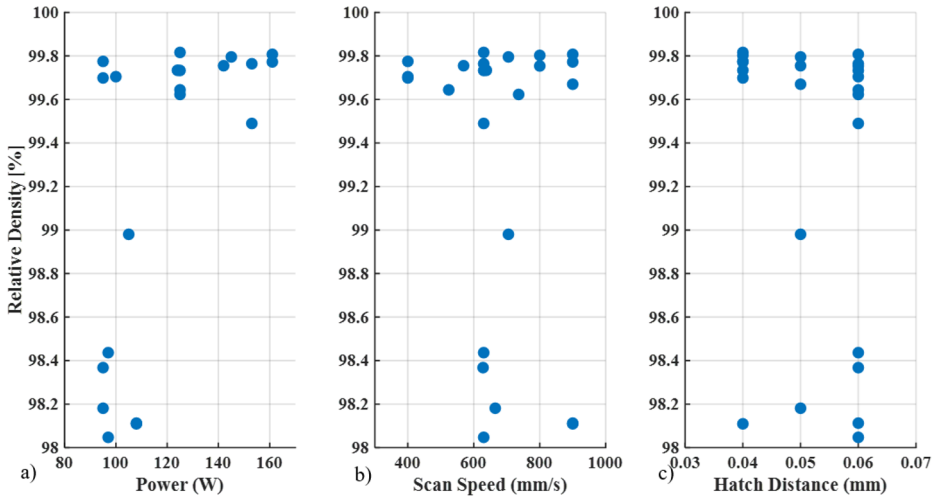

Fig. 4. Scatter plot of a) effect of power b) effect of scan speed and c) effect of hatch spacing on RD.

While the figure above provides some insight into the effect of each parameter on RD alone, the relationship between VED and RD is depicted in Figure 5 below. A clear trend was observed in which samples processed with a VED below approximately 103 J/mm³ consistently exhibited lower RD values, clustering between 98.0% and 98.8%. These points, particularly dominated by the red and blue dots (representing 0.06 mm and 0.05 mm h values), indicate that the energy applied is insufficient for proper melting leading to LOF porosity as illustrated in Figure 6.

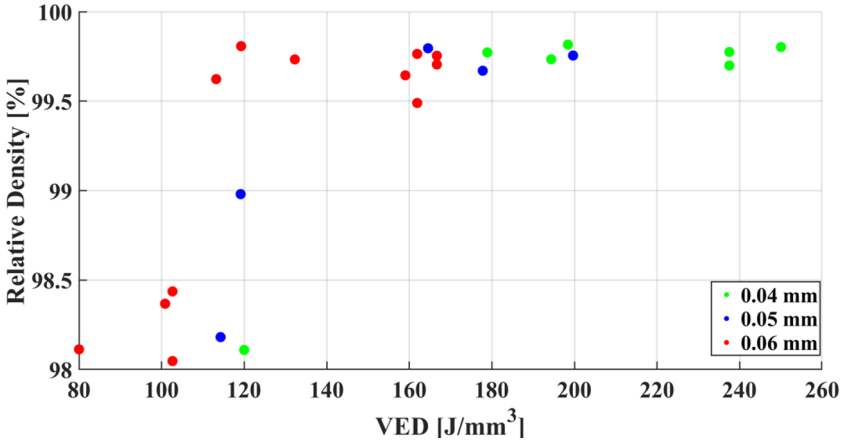

Fig. 5. RD versus VED with green dots = 0.040 m hatch distance, blue dots = 0.050 mm hatch distance and red dots = 0.060 mm hatch distance.

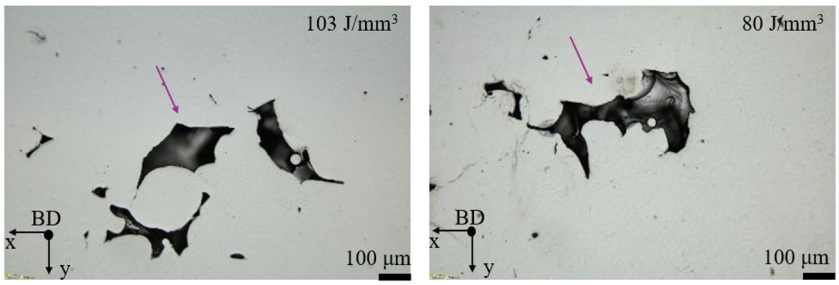

Fig. 6. OM micrographs of LOF pores in low VED samples, indicated with a purple arrow.

As the VED increased beyond 120 J/mm³, the RD improved substantially, with most values rising above 99.5%. This transition marked a threshold beyond which sufficient energy was available to achieve full melting and consistent interlayer bonding. Notably, this improvement was consistent across all h values, indicating that VED was the dominant factor influencing densification in this region. Beyond 160–180 J/mm³, RD values appeared to stabilise, consistently exceeding 99.6%, suggesting that further increases in VED did not result in significant gains in density. However, these higher energy inputs may introduce other issues, such as increased residual stresses or microcracking. Based on these findings, the optimal VED range for achieving high RD (>99.6%) without overprocessing was identified to be approximately 160–180 J/mm³. However, within the intermediate VED range of 113.2 to 119.6 J/mm³, the RD values exhibited considerable variability, from a low of 98.11% to a high of 99.79%, despite similar energy input. This variation suggests that VED alone does not adequately capture the complex effects of process parameters on part density, particularly when subtle interactions between P, v, and h influence melt pool dynamics and defect formation.

3.2 Microstructure

A subset of samples exhibiting high RD with varying VED was used to examine the impact of VED on the microstructure. The six selected samples are presented in Table 2, along with their respective relative densities, process parameters, and VED values.

Table 2. Subset of samples for microstructural analysis.

Subset Label	P [W]	v [mm/s]	h [mm]	RD [%]	VED [J/mm³]
L1	125	736	0.06	99.62	113.22
L2	161	900	0.06	99.79	119.26
M1	200	900	0.05	99.67	177.78
M2	125	630	0.04	99.82	198.41
H1	95	400	0.04	99.76	237.50
H2	200	800	0.04	99.81	250.00

In Figure 7 below, the OM micrographs of the six samples' horizontal plane are illustrated. The analysis indicates that at elevated and medium values of VED, both microcracks and keyhole defects are prevalent. This suggests a correlation between higher energy input during the manufacturing process and the emergence of these defects, likely due to excessive heat leading to rapid cooling and solidification. In contrast, at lower VEDs, the absence of visible cracks points to a more controlled solidification process, which promotes better structural cohesion and integrity, as corroborated by other literature as well [34].

Notably, the sample designated L1 (P125S736H60) exhibited a unique defect profile, characterised by a LOF defect in addition to the keyholing observed. The presence of a LOF defect indicates areas where the material has not fully melted or fused during the process, potentially leading to defects in the final product. This consolidation of keyholing and LOF underscores the critical balance required in energy input during fabrication, highlighting the

need for careful optimisation of VED to minimise defects and ensure optimal material properties.

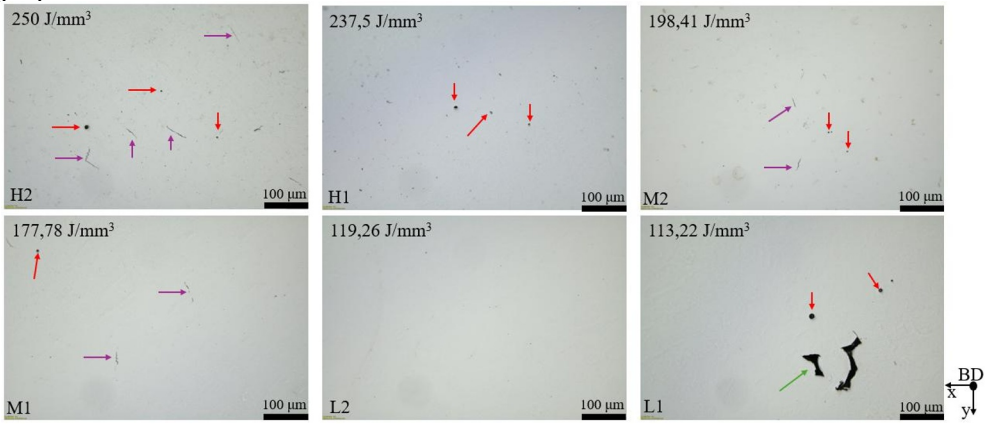

Fig. 7. OM micrographs of subset samples' defect formation, with red arrows indicating keyholing, purple arrows indicating micro cracks and green arrows indicating LOF defects.

The longitudinal planes of samples M1(P200S900H50), M2 (P125S630H40), and L2 (P161S900H60) were analysed using OM and SEM, as illustrated in the accompanying Figure 8 and Figure 9, respectively. The analysis revealed no significant differences in the microstructure of cross-sections of the three samples. The presence of cellular and columnar grains, a common characteristic feature associated with LPBF, is observed in all samples.

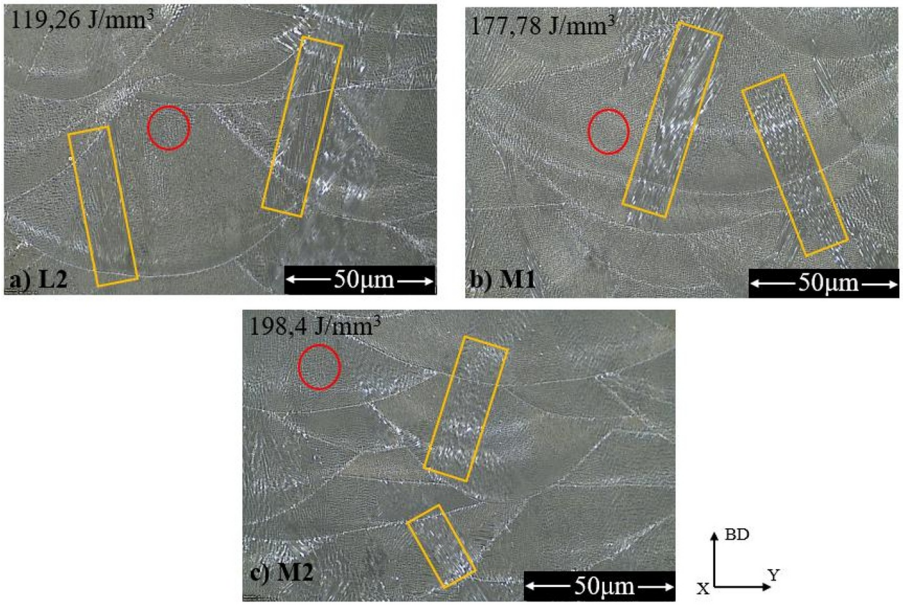

Fig. 8. a) to c) OM micrographs of the longitudinal plane with a red circle indicating the cellular structure and an orange triangle indicating the columnar structure.

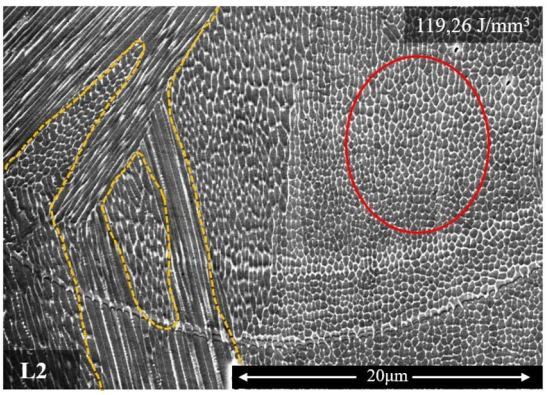

Fig. 9: SEM 8,000 x magnification of the longitudinal plane of sample L2, highlighting cellular (red) and columnar (orange) structures.

4 Discussion

4.1 Density

The impact of pore defects on mechanical properties is detrimental due to stress concentrations that promote crack initiation and propagation [8]. The v, P, h, and t play decisive roles in the density and microstructural features of the final product, which need to be thoroughly investigated in order to optimise the LPBF process. The results achieved in this study show that samples comprising a VED of 119 J/mm³ resulted in a RD of 99.79, 98.99, and 98.13%, which included LOF pores in samples with a RD below 99%. Liu *et al.*[30] similarly observed that variations in the P and v ratios affect the porosity and microstructure when the same VED is applied. The study concluded that these differences are attributed to changes in the cooling rates of the melt pool, even when the VED remains constant [30].

4.1.1 Evaluating alternative predictors of RD beyond VED

To better understand which parameter combinations might more accurately predict RD at a VED of 119 J/mm³, the thermal behaviour during LPBF was considered for further insight. Literature often uses normalised enthalpy (ΔH) as a dimensionless parameter to characterise the heat input during processing that combines P , v , beam spot size (σ), laser penetration depth (η), and material properties to characterise such as; and material properties such as specific heat capacity (C), density (ρ), viscosity (μ), and thermal diffusivity (α) as illustrated in equation 3 below [35].

Bertolli *et al.* [36] employed ΔH to distinguish between conduction and keyholing modes, emphasising that P exerts a greater influence on melt pool depth than other variables. Their study referenced the work of Eager and Tsai, who explained that the peak temperature achieved by a material when heated by a Gaussian-shaped heat source is proportional to the ratio of P to the square root of the v. This relationship suggests that the normalised enthalpy can be proportional to the ratio $P/\sqrt{v}$ as illustrated in Equation 3 [36, 37].

$$\Delta H = \frac{\eta C P}{\rho \sqrt{\alpha v \sigma^3}} \sim \frac{P}{\sqrt{v}}$$

Although ΔH does not incorporate hatch spacing, it was intentionally varied in this study to assess VED's influence on RD and microstructure. Figure 10 plots RD against both VED

and $P/\sqrt{v}$ to evaluate which metric provides stronger correlation, especially in cases where VED lacked predictive accuracy. In Figure 10, $P/\sqrt{v}$ demonstrates a more consistent relationship with RD across all hatch spacings. For example, three data points with nearly identical VED (119 J/mm³) but different h exhibited $P/\sqrt{v}$ values of 3.6, 3.95, and 5.37 J·s$^{0.5}$/mm$^{0.5}$, resulting in RD values of 98.11%, 98.98%, and 99.81%, respectively. Despite having the same VED, the spread in RD highlights that VED, being a volumetric approximation, fails to capture the nonlinear thermal dynamics of LPBF [36, 38]. In contrast, $P/\sqrt{v}$ offers a more physically representative parameter by incorporating the nonlinear influence of v on heat input. $P/\sqrt{v}$ more directly reflects the rate at which thermal energy is supplied relative to the time available for heat conduction and melt pool stabilisation. This makes it more sensitive to melt pool behaviour and solidification dynamics, both of which critically influence porosity formation and, ultimately, the final part density. Therefore, $P/\sqrt{v}$ can provide a more accurate and predictive metric for process optimisation in LPBF.

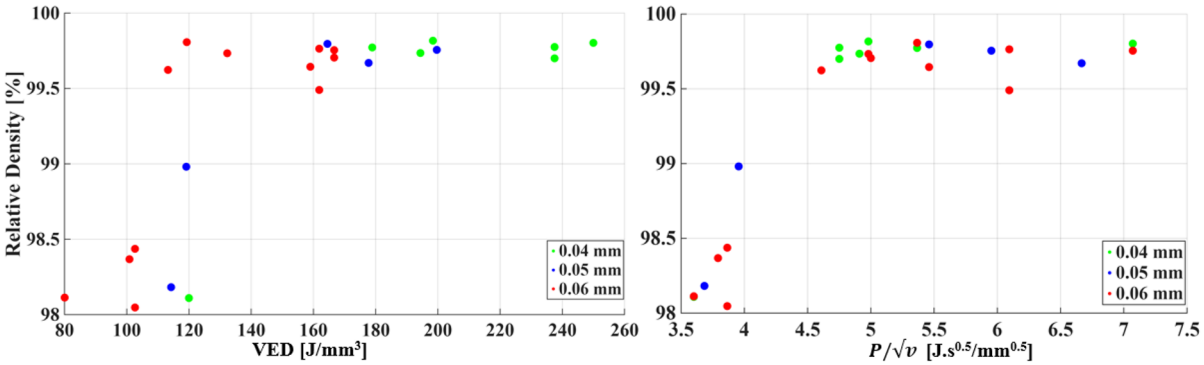

Fig. 10. RD vs VED (left hand side) RD vs $P/\sqrt{v}$ (right hand side) with green dots = 0.04mm hatch distance, blue dots = 0.05mm hatch distance and red dots = 0.06mm hatch distance.

The parameter set with the highest RD (99.82%) comprised P = 125 W, v = 630 mm/s, and h = 0.04 mm, corresponding to $P/\sqrt{v}$ = 4.98 J·s$^{0.5}$/mm$^{0.5}$ and VED = 198.41 J/mm³. However, despite the high density, this sample exhibited microcracks (Figure 11a). Cracks can severely degrade fatigue and fracture resistance by acting as stress concentrators, or stress risers. In contrast, the second-highest RD (99.79%) was achieved using P = 161 W, v = 900 mm/s, and h = 0.06 mm, with a higher $P/\sqrt{v}$ of 5.37 J·s$^{0.5}$/mm$^{0.5}$ but a lower VED of 119 J/mm³. Notably, this sample did not show any visible cracking (Figure 11b).

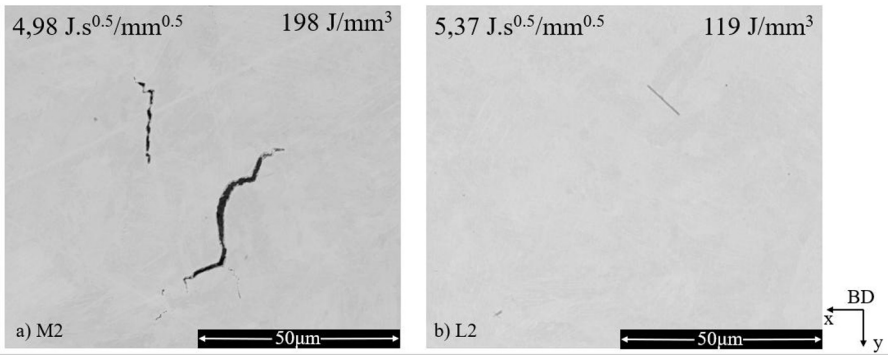

Fig. 11. SEM images at 3000 x magnification of a) the highest density achieved, with micro cracks, and b) the second highest density achieved with no cracks.

The contrasting outcomes observed, where one sample with high RD exhibited cracking while another with a similar RD did not, underscore the limitations of relying solely on VED as a predictor of defect formation. To further explore this limitation, Figure 12 illustrates RD plotted against VED, with samples categorised by the type of defect observed. As indicated, the yellow region, which encompasses mid-to-high VED values, includes both cracked and crack-free samples, thus demonstrating that VED alone lacks the sensitivity needed to reliably differentiate between cracking and non-cracking regimes.

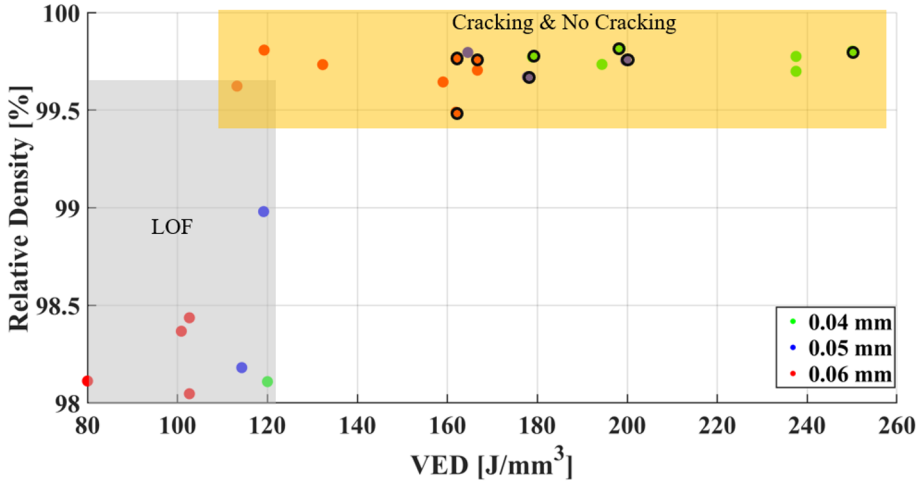

Fig. 12. RD vs VED showing categorised defect regimes: LOF (grey) and "Cracking & No Cracking" (yellow) with samples exhibiting cracks circled in black.

In contrast, Figure 13 plots RD against $P/\sqrt{v}$, for each h value individually. A more distinct separation is observed between the LOF and cracking zones across all h values, demonstrating that $P/\sqrt{v}$ offers a clearer correlation with defect types. This supports the conclusion that $P/\sqrt{v}$ is a more physically representative metric for capturing the thermal conditions that govern defect formation in LPBF, particularly in relation to cracking. However, it is important to note that $P/\sqrt{v}$ does not account for h, which may influence the onset of cracking. Based on the data presented, samples with a similar $P/\sqrt{v}$ value; for example, around 5 J·s$^{0.5}$/mm$^{0.5}$ samples begin to show cracking when the h is smaller and no cracking when h is increased. This likely due to increased thermal overlap and accumulated residual stresses. This suggests that h plays a secondary but significant role in defining the transition between defect regimes.

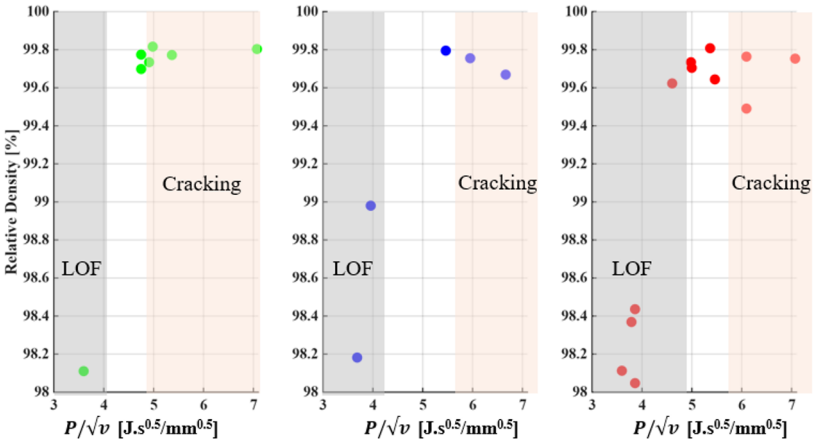

Fig. 13. RD vs $P/\sqrt{v}$ for hatch spacings: (left) 0.04 mm, (middle) 0.05 mm, (right) 0.06 mm. LOF and cracking regimes shaded for clarity.

4.2 Microstructure

4.2.1 VED effect on microstructure

Due to the complexity of CoCrMo alloying system, results reported in literature regarding the as-built microstructure have been inconsistent. The majority of literature indicates that the predominant phase present in the as-built state of LPBF CoCrMo is the γ-phase [25-27, 39-41]. Literature has shown that the unidirectional heat dissipation in LPBF promotes the epitaxial growth of columnar grains, resulting in a typical <100> crystallographic texture along the building direction [42].

Upon examining the XRD patterns of the analysis subset shown in Figure 14, the presence of a γ-phase is confirmed. Dominant reflections are observed from the (111), (020), and (022) planes, exhibiting high intensity at 2θ values of 51.51°, 60.11°, and 90.23. Notably, a distinct variation in peak intensities with changing VED suggests a shift in preferred crystallographic orientation. At high and medium VED levels, the (020) peak exhibits distinctly higher intensity relative to the (111) and (022) peaks, indicating a stronger <100> texture along the build direction.

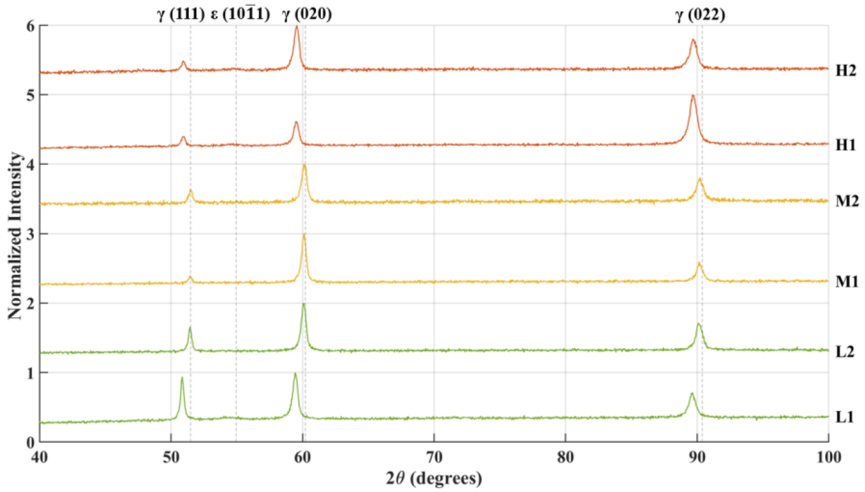

Fig. 14. XRD diffraction profile of subset as described in Table 2.

These profiles indicate that VED influences crystallographic texture and residual stress. As VED increased from sample L1 (P125S736H60) to H2 (P200S800H40), the diffraction patterns exhibited a clear enhancement of <100> texture, suggesting that higher energy input favours grain growth aligned with the deposition direction. This is consistent with directional solidification driven by higher thermal gradients. In contrast, the two low-VED samples, L1 and L2 (P161S900H60), displayed stronger (111) reflections, indicative of a <111> texture. Similar texture behaviour in response to thermal input has been reported in alloys such as Hastelloy-X [43].

In terms of texture, the presence of a predominant (111) plane in the microstructure enhances the material's ductility, when loaded uniaxially. This plane is a close-packed plane, promoting slip in the <110> directions, which is favourable for mechanical properties such as fatigue and ductility.

In addition to variations in peak intensities, a subtle shift in diffraction peak positions is observed across samples with different VED levels. This shift suggests changes in the lattice parameters, which may be attributed to thermal stresses resulting in residual strain, or compositional variations introduced during the LPBF process. Considering samples H1 (P95S400H40), H2 (P200S800H40) and L1 (P125S736H60), the peaks appear slightly displaced toward lower 2θ angles, indicating lattice expansion, potentially due to higher retained thermal stresses or increased solute trapping during rapid solidification. Conversely, samples M1 (P200S900H50), M2 (P125S630H40) and L2 (P161S900H60) show peak positions closer to the expected equilibrium positions, implying reduced internal stress or partial relaxation. Such peak shifts are characteristic of the complex thermal cycles in LPBF and highlight how VED influences not only defect structures and microstructural texture but also the microstrain and crystal lattice itself [44].

This observation has also been noted in other LPBF materials, such as commercially pure titanium. Gu *et al*. [44] concluded that changing v caused peak shifts in commercially pure titanium, which they attributed to martensitic phase transformations. While solidification rate plays a key role, residual stresses were also suggested to contribute to the observed diffraction behaviour [45]. Overall, the current study's results demonstrate that variations in VED not only influence defect formation and porosity but also alter crystallographic texture and lattice strain, which are likely to affect the mechanical anisotropy and surface properties of LPBF processed CoCrMo components.

4.2.2 Parameter effect on microstructure

To investigate the influence of various processing parameters on the microstructure, samples were strategically selected from the design space, each characterised by differing processing conditions. The relevant process parameters associated with each sample are presented in Table 3.

Table 3. Process parameter effect on microstructure subset.

Label	P [W]	v [mm/s]	h [mm]	$P/\sqrt{v}$ [J.s$^{0.5}$/mm$^{0.5}$]	VED [J/mm^3]
P1	153	630	0.06	6.10	161.90
P2	97	630	0.06	3.86	102.65
S1	125	736	0.06	4.61	113.22
S2	125	630	0.06	4.98	132.28
HD1	200	800	0.06	7.07	166.67
HD2	200	800	0.04	7.07	250.00

From Figure 15, the effect that parameters have on the microstructure is clear; with P and v having the largest effect on the microstructure. The change in peak intensities justifies the effect. The shift in intensities from high P (156 W) to low P (97 W) indicates that a higher P might contribute to the γ (022) phase formation when compared to the γ (111) phase.

The effect that v has on the microstructure illustrates that lowering the scan speed from 736 to 630 mm/s stimulates the growth of the ε-phase. Similar findings have been reported in studies, suggesting that a slower scan speed may reduce the cooling rate, allowing the ε-phase to form during solidification [30]. In contrast, the hatch distance does not significantly affect the microstructure, as both 0.06 and 0.04 mm hatch distances produce the same microstructure.

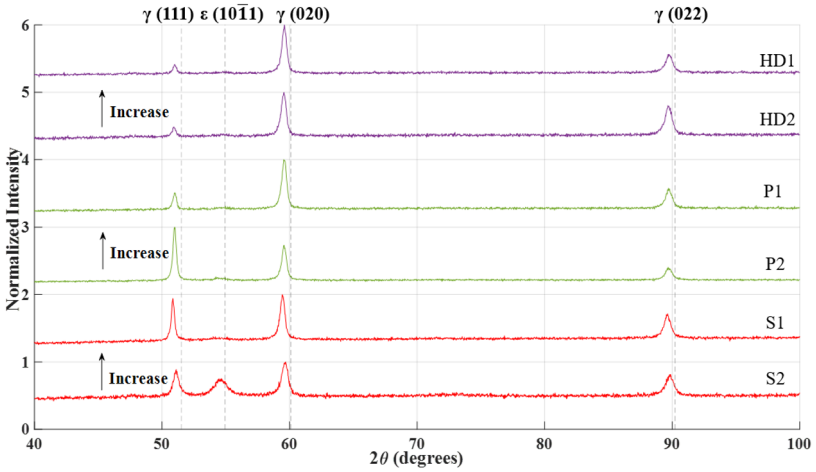

Fig. 15. Effect of parameters on microstructure; red lines - effect of v , green lines - effect of P, purple lines, effect of h .

5 Conclusions

This study aimed to investigate the influence of VED on the density and microstructure of additively manufactured CoCrMo using LPBF. It was demonstrated that VED provide insight into broadly determining parameters to obtain high density. For the VED range of 113.2 to 119.6 J/mm^3, the RD varied from 98.11 to 99.81 % with samples comprising LOF pores, key holes and cracks. The highest density was recorded with a VED of 198 J/mm^3, however, upon further investigation, the sample comprised cracks, whereas the sample with a VED of 119 J/mm^3 provided high density with no observed cracks.

It was found that VED has an effect on the microstructural texture and microstrain of the samples, with high and medium VED levels, a strong <100> texture is observed along the build direction, a characteristic often associated with directional solidification and epitaxial grain growth under steep thermal gradients. In contrast, low VED samples show a strong <111> orientation, suggesting potential reorientation due to slower melt pool dynamics. Lastly, the effect of parameters was investigated, and it was found that P and v play a significant role, with an increase in P and v contributing to a <100> directional growth. In contrast, h had minimal to no effect on the microstructural features of LPBF CoCrMo.

6 Recommendations

Future work should conduct EBSD and neutron diffraction on samples to corroborate the XRD findings and provide deeper insight into microstructure texture. The effect of normalised enthalpy on mechanical properties, as measured by tensile testing or hardness testing, should be investigated.

The study team would like to express gratitude to the Laboratory for Analytical Services at NWU for their assistance with the XRD analysis, as well as the Laboratory for Electron Microscopy at NWU for their support with the SEM analysis. Lastly, we extend our appreciation for the funding provided by CPAM, which made this research possible.

References

[1] B. Blakey-Milner, P. Gradl, G. Snedden, M. Brooks, J. Pitot, E. Lopez, M. Leary, F. Berto, and A. du Plessis, Metal additive manufacturing in aerospace: A review, Mater. Des. **209**, (2021). http://dx.10.1016/j.matdes.2021.110008.org/

[2] N. T. Aboulkhair, N. M. Everitt, I. Ashcroft, and C. Tuck, Reducing porosity in AlSi10Mg parts processed by selective laser melting, Addit. Manuf. **1-4**, 77-86 (2014). http://dx.10.1016/j.addma.2014.08.001.org/

[3] Q. Jia and D. Gu, Selective laser melting additive manufacturing of Inconel 718 superalloy parts: Densification, microstructure and properties, J. Alloys Compd. **585**, 713-721 (2014). http://dx.10.1016/j.jallcom.2013.09.171.org/

[4] L. Thijs, F. Verhaeghe, T. Craeghs, J. V. Humbeeck, and J.-P. Kruth, A study of the microstructural evolution during selective laser melting of Ti–6Al–4V, Acta. Mater. **58**, 3303-3312 (2010). http://dx.10.1016/j.actamat.2010.02.004.org/

[5] J. S. Saini, L. Dowling, D. Trimble, and D. Singh, Mechanical Properties of Selective Laser Melted CoCr Alloys: A Review, J. Mater. Eng. Perform. **30**, 8700-8714 (2021). http://dx.10.1007/s11665-021-06283-1.org/

[6] S. Banerjee, G. Kulesha, M. Kester, and M. A. Mont, Emerging Technologies in Arthroplasty: Additive Manufacturing, J. Knee Surg. (2014). http://dx.10.1055/s-0034-1374810.org/

[7] Y. Duan, X. Liu, S. Zhang, L. Wang, F. Ding, S. Song, X. Chen, B. Deng, and Y. Song, Selective Laser Melted Titanium Implants Play a Positive Role in Early Osseointegration in Type 2 Diabetes Mellitus Rats, Dent. Mater. J. (2020). http://dx.10.4012/dmj.2018-419.org/

[8] Y. He, D. Burkhalter, D. B. Durocher, and J. M. Gilbert, "Solid-Lattice Hip Prosthesis Design: Applying Topology and Lattice Optimization to Reduce Stress Shielding From Hip Implants," in Proceedings of the 2018 Design of Medical Devices Conference, Minneapolis, Minnesota, USA, April 9–12 (2018)

[9] J. Matena, S. Petersen, M. Gieseke, A. Kampmann, M. Teske, M. Beyerbach, H. M. Escobar, H. Haferkamp, N.-C. Gellrich, and I. Nolte, SLM Produced Porous

Titanium Implant Improvements for Enhanced Vascularization and Osteoblast Seeding, Int. J. Mol. Sci. (2015). http://dx.10.3390/ijms16047478.org/

[10] L. Mullen, R. Stamp, W. Brooks, E. S. Jones, and C. Sutcliffe, Selective Laser Melting: A Regular Unit Cell Approach for the Manufacture of Porous, Titanium, Bone In-growth Constructs, Suitable for Orthopedic Applications, J. Biomed. Mater. Res. B Appl. Biomater. (2008). http://dx.10.1002/jbm.b.31219.org/

[11] S. A. Naghavi, M. Tamaddon, P. Garcia-Souto, M. Moazen, S. W. Taylor, J. Hua, and C. Liu, A Novel Hybrid Design and Modelling of a Customised Graded Ti-6Al-4v Porous Hip Implant to Reduce Stress-Shielding: An Experimental and Numerical Analysis, Frontiers in Bioengineering and Biotechnology (2023). http://dx.10.3389/fbioe.2023.1092361.org/

[12] Y. Okazaki and J. Mori, Mechanical Performance of Artificial Hip Stems Manufactured by Hot Forging and Selective Laser Melting Using Biocompatible Ti-15Zr-4Nb Alloy, Materials (2021). http://dx.10.3390/ma14040732.org/

[13] W. Peng, L. Xu, J. You, L. Fang, and Q. Zhang, Selective Laser Melting of Titanium Alloy Enables Osseointegration of Porous Multi-Rooted Implants in a Rabbit Model, Biomedical Engineering Online (2016). http://dx.10.1186/s12938-016-0207-9.org/

[14] M. Tsukanaka, S. Fujibayashi, M. Takemoto, T. Matsushita, T. Nakamura, K. Sasaki, and S. Matsuda, Bioactive Treatment Promotes Osteoblast Differentiation on Titanium Materials Fabricated by Selective Laser Melting Technology, Dent. Mater. J. (2016). http://dx.10.4012/dmj.2015-127.org/

[15] S. Xiang, Y. Yuan, C. Zhang, and J. Chen, Effects of Process Parameters on the Corrosion Resistance and Biocompatibility of Ti6Al4V Parts Fabricated by Selective Laser Melting, Acs Omega (2022). http://dx.10.1021/acsomega.1c06246.org/

[16] J. Yang, X. Yu, Z. Zhang, R. Xu, F. Wu, T. Wang, Y. Liu, J. Ouyang, and F. Deng, Surface Modification of Titanium Manufactured Through Selective Laser Melting Inhibited Osteoclast Differentiation Through Mitogen-Activated Protein Kinase Signaling Pathway, J. Biomater. Appl. (2020). http://dx.10.1177/0885328220920457.org/

[17] K. G. Prashanth, S. Scudino, and J. Eckert, Defining the tensile properties of Al-12Si parts produced by selective laser melting, Acta. Mater. **126**, 25-35 (2017). http://dx.https://doi.org/10.1016/j.actamat.2016.12.044.org/

[18] B. AlMangour, M. Luqman, D. Grzesiak, H. Al-Harbi, and F. Ijaz, Effect of processing parameters on the microstructure and mechanical properties of Co–Cr–Mo alloy fabricated by selective laser melting, Mater. Sci. Eng. A **792**, (2020). http://dx.10.1016/j.msea.2020.139456.org/

[19] B. Zhang, Y. Li, and Q. Bai, Defect Formation Mechanisms in Selective Laser Melting: A Review, Chinese Journal of Mechanical Engineering (English Edition) **30**, 515-527 (2017). http://dx.10.1007/s10033-017-0121-5.org/

[20] I. Yadroitsev, Selective laser melting: Direct manufacturing of 3D-objects by selective laser melting of metal powders, (2009)

[21] H. Y. Chia, J. Wu, X. Wang, and W. Yan, Process parameter optimization of metal additive manufacturing: a review and outlook, J. Mater. Info. **2**, 16-16 (2022). http://dx.10.20517/jmi.2022.18.org/

[22] L. Tonelli, A. Fortunato, and L. Ceschini, CoCr alloy processed by Selective Laser Melting (SLM): effect of Laser Energy Density on microstructure, surface morphology, and hardness, J. Manuf. Process. **52**, 106-119 (2020). http://dx.10.1016/j.jmapro.2020.01.052.org/

[23] A. Matos Da Silva Costa, J. P. Oliveira, A. Luiz, J. Munhoz, E. Guimarães, B. Leite, D. Souza De Freitas, M. De, J. Monteiro, and J. Rodriguez, Co-Cr-Mo alloy fabricated by laser powder bed fusion process: grain structure, defect formation, and mechanical properties, http://dx.10.1007/s00170-021-07570-w/Published.org/

[24] K. P. Gupta, The Co-Cr-Mo (cobalt-chromium-molybdenum) system, **26**, 87-92 (2005)

[25] Y. Kajima, A. Takaichi, T. Nakamoto, T. Kimura, Y. Yogo, M. Ashida, H. Doi, N. Nomura, H. Takahashi, T. Hanawa, and N. Wakabayashi, Fatigue strength of Co-Cr-Mo alloy clasps prepared by selective laser melting, J. Mech. Behav. Biomed. Mater. **59**, 446-458 (2016). http://dx.10.1016/j.jmbbm.2016.02.032.org/

[26] L. H. M. Antunes, J. J. Hoyos, E. B. Fonseca, M. Béreš, P. F. da Silva Farina, E. S. N. Lopes, A. L. Jardini, and R. M. Filho, Effect of phase transformation on ductility of additively manufactured Co–28Cr–6Mo alloy: An in situ synchrotron X-ray diffraction study during mechanical testing, Mater. Sci. Eng. A **764**, (2019). http://dx.10.1016/j.msea.2019.138262.org/

[27] S. L. Sing, S. Huang, and W. Y. Yeong, Effect of solution heat treatment on microstructure and mechanical properties of laser powder bed fusion produced cobalt-28chromium-6molybdenum, Mater. Sci. Eng. A **769**, (2020). http://dx.10.1016/j.msea.2019.138511.org/

[28] M. Zhang, Y. Yang, C. Song, Y. Bai, and Z. Xiao, An investigation into the aging behavior of CoCrMo alloys fabricated by selective laser melting, J. Alloys Compd. **750**, 878-886 (2018). http://dx.10.1016/j.jallcom.2018.04.054.org/

[29] Z. Wang, S. Y. Tang, S. Scudino, Y. P. Ivanov, R. T. Qu, D. Wang, C. Yang, W. W. Zhang, A. L. Greer, J. Eckert, and K. G. Prashanth, Additive manufacturing of a martensitic Co–Cr–Mo alloy: Towards circumventing the strength–ductility trade-off, Addit. Manuf. **37**, (2021). http://dx.10.1016/j.addma.2020.101725.org/

[30] W. Liu, Q. Xie, Y. Cao, J. Wang, and P. Bai, Optimization of processing parameters for LPBF-manufactured CoCr alloys based on laser volume energy density, J. Mater. Res. Technol. **27**, 4053-4063 (2023). http://dx.10.1016/j.jmrt.2023.10.268.org/

[31] P. Mercelis and J. P. Kruth, Residual stresses in selective laser sintering and selective laser melting, Rapid Prototyping Journal **12**, 254-265 (2006). http://dx.10.1108/13552540610707013.org/

[32] T. de Terris, O. Andreau, P. Peyre, F. Adamski, I. Koutiri, C. Gorny, and C. Dupuy, Optimization and comparison of porosity rate measurement methods of Selective Laser Melted metallic parts, Addit. Manuf. **28**, 802-813 (2019). http://dx.10.1016/j.addma.2019.05.035.org/

[33] K. Geels, Metallographic and Materialographic Specimen Preparation, Light Microscopy, Image Analysis and Hardness Testing, (2007)

[34] C. Li, Q. Zhang, Y. Ren, W. Chen, W. Li, J. Chen, and L. Zhou, Influence of energy density on the microstructure and property regulation of additive manufactured pure nickel, Advances in Mechanical Engineering **16**, (2024). http://dx.10.1177/16878132241230228.org/

[35] W. E. King, H. D. Barth, V. M. Castillo, G. F. Gallegos, J. W. Gibbs, D. E. Hahn, C. Kamath, and A. M. Rubenchik, Observation of keyhole-mode laser melting in laser powder-bed fusion additive manufacturing, J. Mater. Process. Technol. **214**, 2915-2925 (2014). http://dx.10.1016/j.jmatprotec.2014.06.005.org/

[36] U. Scipioni Bertoli, A. J. Wolfer, M. J. Matthews, J.-P. R. Delplanque, and J. M. Schoenung, On the limitations of Volumetric Energy Density as a design parameter for Selective Laser Melting, Mater. Des. **113**, 331-340 (2017). http://dx.10.1016/j.matdes.2016.10.037.org/

[37] T. W. Eagar and N. S. Tsai, TEMPERATURE FIELDS PRODUCED BY TRAVELING DISTRIBUTED HEAT SOURCES, Weld. J. **62**, 346-355 (1983). http://dx.scopus.com/pages/publications/0020880803?inward=#tab=similar.org/

[38] T. Yang, T. Liu, W. Liao, E. MacDonald, H. Wei, C. Zhang, X. Chen, and K. Zhang, Laser powder bed fusion of AlSi10Mg: Influence of energy intensities on spatter and porosity evolution, microstructure and mechanical properties, J. Alloys Compd. **849**, (2020). http://dx.10.1016/j.jallcom.2020.156300.org/

[39] A. Takaichi, Y. Kajima, N. Kittikundecha, H. L. Htat, H. H. Wai Cho, T. Hanawa, T. Yoneyama, and N. Wakabayashi, Effect of heat treatment on the anisotropic microstructural and mechanical properties of Co-Cr-Mo alloys produced by selective laser melting, J Mech Behav Biomed Mater **102**, 103496 (2020). http://dx.10.1016/j.jmbbm.2019.103496.org/

[40] Z. Chen, Z. Xia, Y. Cheng, Y. Song, T. Wei, C. Ge, C. Lu, C. Wang, X. Zhu, and Q. Jia, New insights into the mechanical property anisotropy of CoCrMo alloy fabricated by laser powder bed fusion (LPBF), Mater. Sci. Eng. A **925**, (2025). http://dx.10.1016/j.msea.2025.147878.org/

[41] M. Roudnická, O. Molnárová, J. Drahokoupil, J. Kubásek, J. Bigas, V. Šreibr, D. Paloušek, and D. Vojtěch, Microstructural instability of L-PBF Co-28Cr-6Mo alloy at elevated temperatures, Addit. Manuf. **44**, (2021). http://dx.10.1016/j.addma.2021.102025.org/

[42] Z. W. Chen, M. A. L. Phan, and K. Darvish, Grain growth during selective laser melting of a Co–Cr–Mo alloy, J. Mater. Sci. **52**, 7415-7427 (2017). http://dx.10.1007/s10853-017-0975-z.org/

[43] S. Zhang, Y. Lei, Z. Chen, P. Wei, W. Liu, S. Yao, and B. Lu, Effect of Laser Energy Density on the Microstructure and Texture Evolution of Hastelloy-X Alloy Fabricated by Laser Powder Bed Fusion, Materials (Basel) **14**, (2021). http://dx.10.3390/ma14154305.org/

[44] D. Gu, Y.-C. Hagedorn, W. Meiners, G. Meng, R. J. S. Batista, K. Wissenbach, and R. Poprawe, Densification behavior, microstructure evolution, and wear performance of selective laser melting processed commercially pure titanium, Acta. Mater. **60**, 3849-3860 (2012). http://dx.https://doi.org/10.1016/j.actamat.2012.04.006.org/

[45] J. L. Bartlett and X. Li, An overview of residual stresses in metal powder bed fusion, Addit. Manuf. **27**, 131-149 (2019). http://dx.10.1016/j.addma.2019.02.020.org/

7 Annexures

Table 4. Printing parameters of the study.

				Relative Density [%]			
Sample Nr	**Power [W]**	**Scan Speed [mm/s]**	**Hatch Distancing [mm]**	**1st Quartile**	**Median**	**3rd Quartile**	**VED [J/mm³]**
1	161	900	0.040	99.75	99.76	99.80	178.89
2	142	569	0.050	99.74	99.75	99.77	199.65
3	124	638	0.040	99.71	99.72	99.74	194.36
4	95	400	0.040	99.69	99.71	99.72	237.50
5	95	400	0.040	99.75	99.76	99.77	237.50
6	200	800	0.040	99.79	99.81	99.81	250.00
7	95	628	0.060	98.36	98.36	98.37	100.85
8	161	900	0.060	99.79	99.79	99.83	119.26
9	100	400	0.060	99.71	99.71	99.71	166.67
10	200	900	0.050	99.66	99.67	99.68	177.78
11	108	900	0.040	98.10	98.13	98.13	120.00
12	200	800	0.060	99.75	99.75	99.76	166.67
13	95	665	0.050	98.18	98.18	98.19	114.29
14	108	900	0.060	98.10	98.11	98.12	80.00
15	125	630	0.040	99.79	99.82	99.84	198.41
16	125	524	0.060	99.63	99.63	99.65	159.03
17	145	705	0.050	99.78	99.81	99.81	164.54
18	125	736	0.060	99.62	99.62	99.62	113.22
19	105	705	0.050	98.97	98.99	99.00	119.15
20	125	630	0.060	99.72	99.74	99.74	132.28
21	153	630	0.060	99.48	99.48	99.49	161.90
22	153	630	0.060	99.75	99.78	99.78	161.90
23	97	630	0.060	98.42	98.44	98.45	102.65
24	97	630	0.060	98.04	98.05	98.06	102.65